

## Ultrarelativistic-Positron-Beam Transport through Meter-Scale Plasmas

M. J. Hogan,<sup>1</sup> C. E. Clayton,<sup>2</sup> C. Huang,<sup>2</sup> P. Muggli,<sup>3</sup> S. Wang,<sup>2</sup> B. E. Blue,<sup>2</sup> D. Walz,<sup>1</sup> K. A. Marsh,<sup>2</sup> C. L. O'Connell,<sup>1</sup> S. Lee,<sup>3</sup> R. Iverson,<sup>1</sup> F.-J. Decker,<sup>1</sup> P. Raimondi,<sup>1</sup> W. B. Mori,<sup>2</sup> T. C. Katsouleas,<sup>3</sup> C. Joshi,<sup>2</sup> and R. H. Siemann<sup>1</sup>

<sup>1</sup>Stanford Linear Accelerator Center, Stanford, California 94309, USA

<sup>2</sup>University of California, Los Angeles, California 90095, USA

<sup>3</sup>University of Southern California, Los Angeles, California 90089, USA

(Received 26 November 2002; published 21 May 2003)

We report on the first study of the dynamic transverse forces imparted to an ultrarelativistic positron beam by a long plasma in the underdense regime. Focusing of the 28.5 GeV beam is observed from time-resolved beam profiles after the 1.4 m plasma. The strength of the imparted force varies along the ~12 ps full length of the bunch as well as with plasma density. Computer simulations substantiate the longitudinal aberration seen in the data and reveal mechanisms for emittance degradation.

DOI: 10.1103/PhysRevLett.90.205002

PACS numbers: 52.40.Mj, 41.75.Ht, 41.75.Lx

The interaction of intense positron beams with plasmas has received very little experimental attention compared to that for electron beams. In electron beam transport, an electron bunch can expel all the plasma electrons within its radius on a time scale shorter than the bunch duration. In this underdense or “blowout” regime [1–4], where the peak beam density  $n_{b0}$  is much higher than the plasma density  $n_e$ , a uniform ion channel is created for the remainder of the bunch. Because the transverse fields of an ion channel make a nearly ideal optic, an electron beam can propagate over extended distances in plasmas without substantial emittance degradation. However, for positron beams with  $n_{b0} \gg n_e$ , there is no analogy to blowout. In this “flow-in” regime, background electrons from various distances from the beam will continue to enter the positron beam at various times along the bunch [5]. Moreover, while the ion density  $n_i$  within an electron bunch is limited to the asymptotic value  $n_i = n_e$  after the blowout time, the analogous electron density within a positron bunch can be very much higher than  $n_e$  due to the large reservoir of plasma electrons outside the bunch. Consequently, a positron beam has a stronger and more complex transverse field structure within the bunch and will thus propagate much differently than a similar electron beam. Understanding the differences between the plasma response to an intense positron beam versus a similarly intense electron beam—and the resultant reaction back onto the beam itself as it propagates—is essential to the applications of plasmas in high-energy physics [6,7].

The transport of intense electron bunches through a long (1.4 m), high-density plasma in the blowout regime was recently reported [3]. While plasma focusing of electrons in short plasmas has been observed in a number of experiments in the past, in both the linear [8] and nonlinear regimes [2–4], only recently has the first focusing of an intense positron beam by a short ( $\approx 3$  mm), overdense ( $n_{b0} \ll n_e$ ) plasma been demonstrated [9]. In this Letter, we present the first results of a quantitative

investigation of the propagation of an intense 28.5 GeV positron beam in an extended-length, underdense plasma and compare the results with those obtained by three-dimensional particle-in-cell (PIC) simulations.

The experiment was conducted with the 28.5 GeV positron beam from the linac at the Stanford Linear Accelerator Center. The beam was transported through the Final Focus Test Beam facility (FFTB) and focused at the entrance to the 1.4 m long plasma. Other beam parameters are root mean square (rms) energy spread  $\sigma_E/E \approx 0.4\%$ , particles/bunch =  $(1.8\text{--}2.1) \times 10^{10}$ , invariant emittances  $\epsilon_x(\epsilon_y) \approx 210(150) \times 10^{-6}$  m, rms bunch length  $\sigma_z \approx 0.7$  mm (2.3 ps), and the Twiss parameters  $\beta_x(\beta_y) \approx 2.2(1.9)$  m and  $\alpha_x(\alpha_y) \approx -0.92(-0.03)$ . The beam trajectory and charge were measured using standard FFTB instrumentation while profiles of the beam at three locations near the plasma were measured using imaging systems coupled to charged-coupled device (CCD) cameras, all recorded on a pulse-by-pulse basis [10]. Two profiles are images from optical transition radiators (OTR) located 106 cm upstream of the plasma entrance and 90 cm downstream of the plasma exit. The third profile comes from imaging Cherenkov radiation from a 1 mm thick piece of aerogel onto a CCD. The aerogel was located 11.9 m downstream of the plasma exit and after a bending magnet.

The plasma was produced through single-photon ionization of lithium vapor. The measured energy absorption of the ionizing ultraviolet (UV) laser pulse and the measured cross sectional area of the UV laser beam provide the initial plasma density at the time of photoionization,  $n_e(t=0)$  [11]. The time evolution  $n_e(t)$  is given by  $dn_e(t)/dt = -n_e(t)/\tau_d - \alpha n_e(t)^2$  where  $\tau_d$  is the diffusion time and  $\alpha(n_e)$  is the collisional recombination coefficient [12]. Thus  $n_e(t)$  can be varied by the incident UV energy and/or the delay between the ionizing laser pulse and the positron bunch. The beam profiles obtained from the downstream OTR and Cherenkov radiator for a range of  $n_e(t=0)$  can now be used to empirically determine  $\tau_d$ .

given an estimate for  $\alpha(n_e)$ . For example, the horizontal Cherenkov profile had the same width for delays of  $t = 16$  and  $23 \mu\text{s}$  if the laser energy was 3.3 times larger for the longer delay. It was found that for the low densities of this study, the plasma decay is diffusion dominated with  $\tau_d \approx 12 \mu\text{s}$  and insensitive to the choice of  $\alpha(n_e)$ . From the measured delay time and UV energy,  $n_e(t)$  is known on a shot-by-shot basis.

With the plasma turned off, the emittance-dominated beam profile at the Cherenkov radiator is Gaussian with a typical transverse rms size of  $\approx 0.8 \text{ mm}$  in the non-dispersive ( $x$ ) direction. The beam profile will be highly modified in space and time after propagating through the plasma, where the collective, dynamic forces have altered the trajectory of each positron individually. Since the spatial intensity distribution of the imaged Cherenkov radiation is linear with the transverse and longitudinal profiles of the positron bunch at this Cherenkov plane, sections of the bunch can be time resolved by sending the light to a streak camera. This optical system split and, with  $90^\circ$  rotation and time delay in one of the two arms, recombined the light, forming two orthogonal images on the slit of the  $\approx 1 \text{ ps}$ -resolution streak camera. The  $100 \mu\text{m}$  wide slit captures the time history of  $\approx 300 \mu\text{m}$  wide horizontal and vertical sections through the nominal centroid of the beam at the Cherenkov plane. For the purposes of this study, quantitative data on the time evolution of the nondispersed dimension are studied, while the time centroid of the  $y$  streak is used as a timing fiducial.

Figure 1 shows time-integrated  $x$  spot sizes from the OTR camera downstream of the plasma (squares) and the Cherenkov camera (circles) obtained from Gaussian fits to the  $y$ -integrated images as a function of  $n_e$ . The spot-size minimum at the Cherenkov plane occurs at a density  $n_e \approx 2.0 \times 10^{12} \text{ cm}^{-3}$  while the minimum for the OTR is around  $n_e \approx 7 \times 10^{12} \text{ cm}^{-3}$ . If we consider the plasma as a thick lens, then clearly the focusing strength needed to produce a spot-size minimum increases if the observation plane is closer to the plasma lens. The time-resolved

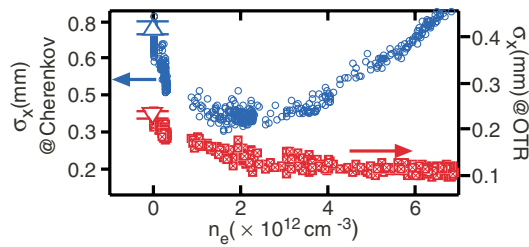


FIG. 1 (color). Time-integrated measurements of the positron beam spot size in the  $x$  direction vs  $n_e$  from the two profile monitors downstream of the plasma exit. The symbols at zero density are the mean no-plasma spot sizes at the Cherenkov radiator ( $\triangle$ ) and OTR ( $\nabla$ ) for 50 pulses. The bars indicate the error of the mean.

focusing was obtained simultaneously for densities up to  $n_e = 3.4 \times 10^{12} \text{ cm}^{-3}$ . The individual streak images were grouped into narrow ( $< \pm 7\%$ ) density bins and the time jitter introduced by the streak camera's trigger electronics was taken out using the  $y$ -streak fiducial. In the following analysis, a single streak record for each density bin was constructed by averaging the images within each bin to improve the photoelectron statistics.

Figure 2 shows data from the streak camera for various densities. Each streak record was sectioned into  $\zeta/c = 1 \text{ ps}$  slices and summed over time at each  $\zeta$ . Here  $\zeta = (ct - z)$  is the longitudinal position along the positron bunch, measured from the peak-current location at  $\zeta = 0$ . The resultant slice data were fit to a Gaussian function providing the time-resolved rms width  $\sigma_x(\zeta)$  as well as the corresponding amplitude of the fit  $A(\zeta)$ . The solid curve in Fig. 2(a) is a Gaussian fit to the  $A(\zeta)$  for  $n_e = 0$  representing the longitudinal current profile of the bunch.

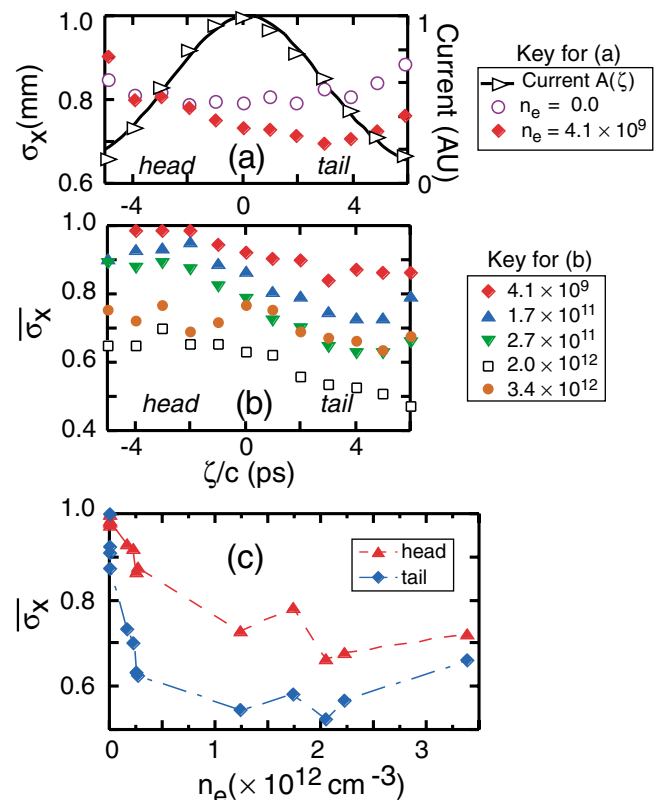


FIG. 2 (color). Time-resolved measurements of the positron bunch at the Cherenkov plane for various plasma densities. (a) Measured bunch intensity  $A(\zeta)$  (right arrows) and Gaussian fit (solid line). Temporal variation  $\sigma_x(\zeta/c)$  of the  $x$  spot size for zero density (circles) and for  $n_e = 4.1 \times 10^9 \text{ cm}^{-3}$  (diamonds). (b) Temporal variation of the normalized  $x$  spot size  $\bar{\sigma}_x(\zeta/c)$  for several densities (see key). Some of the data points for  $\zeta/c = -5$  and  $+6 \text{ ps}$  are close to the noise floor which tends to artificially broaden the slice sizes. (c) Variation with density of  $\bar{\sigma}_x$  for slices at  $-4$  and  $+4 \text{ ps}$ , labeled head and tail, respectively.

Also shown in Fig. 2(a) are the  $\sigma_x(\zeta)$  for no plasma and for  $n_e = 4.1 \times 10^9 \text{ cm}^{-3}$ . Even at this low density, the spot size of slices in the tail of the beam, e.g., around  $\zeta/c$  of +2 to +4 ps, have dropped to <90% of the no-plasma size of about 800  $\mu\text{m}$  while slices in the head of the beam, e.g., around  $\zeta/c$  of -2 to -4 ps, are essentially unchanged. The variation of  $\sigma_x(n_e, \zeta)$  relative to that at zero density is more clearly illustrated by replotted the data with each slice normalized to the spot size of the corresponding slice at  $n_e = 0$ . The  $\sigma_x(\zeta)$  data for  $n_e = 4.1 \times 10^9 \text{ cm}^{-3}$  are replotted as  $\bar{\sigma}_x(\zeta/c)$  with this normalization in Fig. 2(b) along with data from four higher density bins. The three low-density streaks each show continuous head-to-tail focusing. Note that the rate of change of the slice sizes with density is much larger in the tail than at the head of the bunch. The two high-density streaks are at  $n_e = 2.0 \times 10^{12} \text{ cm}^{-3}$ , where the entire bunch is maximally focused, and at  $n_e = 3.4 \times 10^{12} \text{ cm}^{-3}$  where all slices are apparently “overfocused.” Also, while the earliest slices of the full beam should not be focused at all, it appears that it is in the data. However, as can be seen in Fig. 2(a), the data extend only out to where the beam current is about 0.14 of the peak current. Truncation of the streaks at this level was necessary due to the presence of a weak background on the streaks coupled with the intrinsically limited dynamic range of the streak camera when on a ps time scale.

Figure 2(c) summarizes the variation of  $\bar{\sigma}_x(n_e, \zeta/c)$  for  $\zeta/c = -4, 0$ , and +4 ps from 12 density bins. The variation of  $\bar{\sigma}_x(n_e, \zeta/c = -4 \text{ ps})$  is quite slow compared to  $\bar{\sigma}_x(n_e, \zeta/c = +4 \text{ ps})$ . The tail size falls very rapidly up to  $n_e \approx 2.7 \times 10^{11} \text{ cm}^{-3}$  after which it is relatively flat. In fact, beyond this density, the slope of  $\bar{\sigma}_x(n_e, \zeta/c = +4 \text{ ps})/\bar{\sigma}_x(n_e, \zeta/c = -4 \text{ ps})$  changes sign as the head now focuses faster than the tail. For this reason, we will consider  $n_e \approx 2.7 \times 10^{11} \text{ cm}^{-3}$  as that density needed to “optimally focus” the tail of the bunch. Here the tail spot size is primarily emittance limited. At higher densities, we believe that the spot sizes are dominated by radial aberrations. This is borne out in the fact that the tail does not appear to substantially overfocus in proportion to the focusing strength  $\sim \sqrt{n_e}$ —as would be expected for a nonaberrated optic—when the density is raised well beyond  $2.7 \times 10^{11} \text{ cm}^{-3}$ .

It is clear from the three low-density curves in Fig. 2(b) that, since the transverse beam size is dropping with  $\zeta$ , the radial focusing force must be increasing with  $\zeta$ . Evidently the electron density within the beam is also increasing with  $\zeta$ . The requisite density to optimally focus the tail of the positron bunch ( $2.7 \times 10^{11} \text{ cm}^{-3}$ ) is about 7 times lower than for an otherwise identical electron bunch which shows this minimum at  $\approx 2.0 \times 10^{12} \text{ cm}^{-3}$  [3,4]. This is due to the fact that, for the positron case, the charge density of the electrons responsible for the focusing can be much higher than the ambient ion density (the limit for electron bunches).

To obtain further insight into the experimental observations, especially at the higher densities, we use the PIC code QUICKPIC [13]. The code uses the same beam and plasma parameters as in the experiment except for the correlated energy spread on the beam. The image in Fig. 3(a) is a two-dimensional (2D) slice through  $y = 0$  of the normalized charge density  $\eta = [1 - en_e(x, y, \zeta)]/n_i$  surrounding the positron beam, when the beam is near the plasma entrance and  $n_e = 1.0 \times 10^{11} \text{ cm}^{-3}$ . The variation of the electron density within the beam in Fig. 3(a), which is more clearly seen in the accompanying lineouts of Fig. 3(b), shows the increase with  $\zeta$  that was inferred from the time-resolved data of Fig. 2(b). Although the transverse variation of the electron density in the back half of the beam does not provide a unique focusing strength for a given  $\zeta$ , it is nevertheless clear that the focusing is much stronger than for an equivalent electron beam in the blowout regime where  $\eta(x, \zeta \geq 0) = 1$  for  $x$  within the beam. Many of the features in Figs. 3(a) and 3(b) can be qualitatively reproduced by calculating the orbits of plasma electrons starting at various distances  $r_{\text{initial}}$  from the axis of the approaching beam. In addition to the general longitudinal and radial aberration in  $\eta(r, \zeta)$ , such orbit calculations reveal that the spike near  $\zeta = 0$  is due to electrons with  $r_{\text{initial}} \leq \sigma_r$  that reach  $r = 0$  at about the same time (same

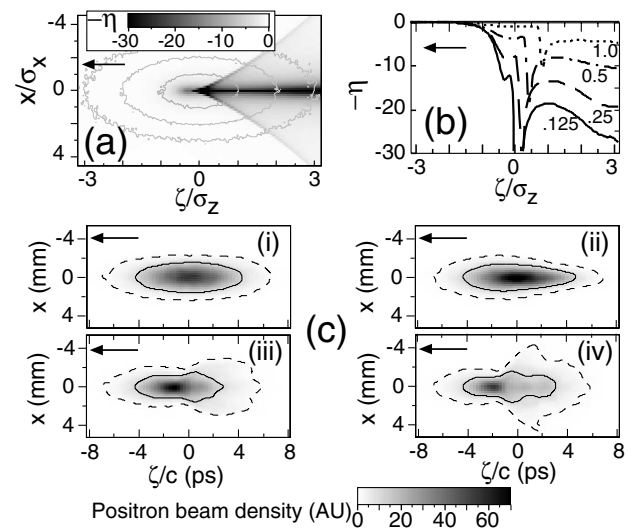


FIG. 3. Results from PIC simulations. The solid arrow in each graph indicates the propagation direction of the bunch. (a) Two-dimensional slice  $\eta(x, y = 0, \zeta)$  ( $\propto$  charge density) at the plasma entrance. The overlay shows the 61%, 22%, and 1% elliptical contours of the beam density. (b) Lineouts of  $\eta(x, y = 0, \zeta)$  for values of  $x/\sigma_x$  of 1, 0.5, 0.25, and 0.125 (moving from the dotted line to the solid line, respectively). (c) Beam intensity plots in the  $x$ - $z$  plane for  $n_e$  values of (i) 0, (ii)  $2.0 \times 10^{11} \text{ cm}^{-3}$ , (iii)  $8.0 \times 10^{11} \text{ cm}^{-3}$ , and (iv)  $2.0 \times 10^{12} \text{ cm}^{-3}$  (see text for details). The solid and dashed contours are at 0.13 and 0.013 of the maximum intensity within all the plots, respectively.

$\zeta$  value) and that the “wings” diverging from the spike are “caustics” where the orbits of electrons that have already crossed the axis, and are being pulled back by the positrons, tend to share a common conical surface. Although the density spike is relatively large, its spatial extent and temporal duration are too small to be seen in the streak data. Finally, we note that these orbit calculations give a scaling for the density enhancement of  $\eta \sim n_{b0}\sigma_z^2$  [14] which follows from the quadratic scaling of the flow-in density with  $r_{\text{initial}}$  and the bunch-length constraint requiring the flow-in time (from  $r_{\text{initial}}$  to  $r = 0$ ) [5] to be  $\sim\sigma_z/c$ .

Figure 3(c) shows four  $x$ - $\zeta$  projections of the positron beam after propagating through plasma of various densities and drifting 12 m to the Cherenkov plane. For these data, the  $y$  integration was over only  $\pm 150 \mu\text{m}$  to model the acceptance of the streak camera slit. As discussed earlier, the limited dynamic range of the streak camera and the low-level background on the streaks forced a truncation of the streak images at about 1/7 of the peak streak signal. We introduce an equivalent “noise floor” into the simulation by plotting contours on top of the relatively high dynamic-range simulation data. The solid contours at 13% of the peak intensity in Fig. 3(c) are thus more representative of the experimental data. The variation of the  $x$  width of this contour for  $2.0 \times 10^{11} \text{ cm}^{-3}$  looks very similar to the experimental data in Fig. 2(b) for a density only 35% higher. Similarly, the variation of the contour width for the  $2.0 \times 10^{12} \text{ cm}^{-3}$  data of Fig. 3(c) is qualitatively the same as the streak data in Fig. 2(b) for the same density. This latter contour follows a narrow feature in the tail of the simulation bunch, even though the tail has clearly overfocused, as can be seen by the dashed contour at the 1.3% intensity level. Although not explicitly explored in the simulations, we believe that the narrow features in the tails are real and due to focusing of off-axis positrons at higher densities.

Figure 3(c) also shows a trend that helps to explain the time-integrated data in Fig. 1. The initial rapid drop in the spot size vs density is due to the strong head-to-tail focusing of the bunch, before any slice has been over-focused. The minimum is nominally where the core of the bunch is maximally focused. The simulation data show that, at this point, the projected beam will have a halo due to the tail particles. Clearly the emittance both for the projected beam and for slices in the tail will be increased by the radial and longitudinal aberrations of the transverse forces from the plasma. The similarity of the experimental data and the PIC code results is quite good considering that the simulation assumes a perfectly axial beam (all slices are centered on the axis of propagation) with no correlated energy spread. The actual beam is imperfect with small head-to-tail tilts and a finite energy spread.

In conclusion, the first detailed study of the dynamics of positron transport through extended-length plasmas

has been presented. By time resolving the spot size of a positron beam downstream of a 1.4 m-long plasma, the dynamic forces imparted by the plasma onto the beam can be inferred. At low densities, longitudinal portions or slices of a bunch are more and more focused as measured from the head to the tail. The tail slices become more tightly focused relative to the head slices as the density is further increased. The density at which the tail slices are optimally focused occurs at  $\sim 1/7$  of the density needed for a similar electron beam. The relative focusing strengths can be understood in terms of the fundamental differences between the plasma response in the “flow-in” and blowout regimes for positron beams and electron beams, respectively. At an even higher density, where the beam evolves substantially while transiting the plasma, the plasma acts as an aberrated, thick plasma lens for the core of the bunch while the positrons in the tail are substantially overfocused. Particle-in-cell codes show reasonable quantitative agreement with the plasma-density scaling of the time-resolved data. The code also predicts that the projected emittance of the positron beam is significantly degraded beyond the plasma lens density. However, launching the positron drive bunch into a hollow plasma channel [5] may minimize some of these deleterious aberrations.

This work is supported by U.S. DoE Grants No. DE-FG03-92ER40745, No. DE-AC03-76SF00515, No. DE-FG03-98DP00211, and No. DEFG03-92ER40727 and by NSF Grants No. ECS-9632735, No. DMS-9722121, and No. PHY-00787157.

- 
- [1] J. B. Rosenzweig *et al.*, Phys. Fluids B **2**, 1376 (1990).
  - [2] N. Barov *et al.*, Phys. Rev. ST Accel. Beams **3**, 011301 (2000).
  - [3] C. E. Clayton *et al.*, Phys. Rev. Lett. **88**, 154801 (2002).
  - [4] C. OConnell *et al.*, Phys. Rev. ST Accel. Beams (to be published).
  - [5] S. Lee *et al.*, Phys. Rev. E **64**, 045501 (2001).
  - [6] P. Chen, Part. Accel. **20**, 171 (1987).
  - [7] S. Lee *et al.*, Phys. Rev. ST Accel. Beams **5**, 011001 (2002).
  - [8] H. Nakanishi *et al.*, Phys. Rev. Lett. **66**, 1870 (1991); G. Hairapetian *et al.*, Phys. Rev. Lett. **72**, 2403 (1994); R. Govil *et al.*, Phys. Rev. Lett. **83**, 3202 (1999).
  - [9] J. S. T. Ng *et al.*, Phys. Rev. Lett. **87**, 244801 (2001).
  - [10] M. Hogan *et al.*, Phys. Plasmas **7**, 2241 (2000).
  - [11] P. Muggli *et al.*, IEEE Trans. Plasma Sci. **27**, 791 (1999).
  - [12] D. R. Bates *et al.*, Proc. R. Soc. London, Ser. A **267**, 19 (1962).
  - [13] C. Huang *et al.*, in *Proceedings of the 2001 Particle Accelerator Conference* (IEEE, Piscataway, NJ, 2001), p. 4005.
  - [14] T. Katsouleas (private communication).